Dissipations in reinforced concrete components: Static and dynamic experimental identification strategy

T. Heitz, A. Le Maoult, B. Richard, Cédric Giry, F. Ragueneau

Dissipations in reinforced concrete components: static and dynamic experimental identification strategy

T. Heitz[a,*], A. Le Maoult[b], B. Richard[b,**], C. Giry[a], F. Ragueneau[a]

[a] *LMT/ENS Cachan/CNRS/Université Paris-Saclay. 61, Avenue du Président Wilson, F-94235, Cachan, France*
[b] *CEA–DEN, Service d'études mécaniques et thermiques (SEMT), Université ParisSaclay, F-91191, Gif-sur-Yvette, France*

Abstract

Despite their now well documented drawbacks, viscous damping based models to describe the dissipations occurring in reinforced concrete (RC) structures during seismic events are popular among structural engineers. Their computational efficiency and their convenient implementation and identification are indeed attractive. Of course, the choice of a viscous damping model is, most of the time, reasonable, but some questions still arise when it comes to calibrate its parameters: how do these parameters evolve through the nonlinear time-history analysis? How do they interact when several eigenmodes are involved? To address these questions, the IDEFIX experimental campaign (French acronym for *Identification of damping/dissipations in RC structural elements*) has been carried out on RC beams set up on the *Azalée* shaking table of the TAMARIS experimental facility operated by the French Alternative Energies and Atomic Energy Commission (CEA). First, this experimental campaign is positioned within an overview of related experimental campaigns in the literature. Second, the IDEFIX experimental campaign is presented. In particular, noticeable results are given by examples of first post-treatments, including an improved so-called "areas method", which lead to very different identified damping ratio depending on the method used.

Keywords: Damping, RC beam, Dissipation, TAMARIS, IDEFIX

1. Introduction

The numerous structural constitutive laws which have been developed since the second part of the 20th century now allow to provide realistic and reliable results on the nonlinear behavior of reinforced concrete (RC) structures. The more complex is the model, the more precise is the required knowledge of the material properties – a knowledge which is not obvious for engineers when the studied structure is still at the design state. Moreover, the variability of these parameters may lead to a necessary extensive numerical study to assess its influence on the structural behavior and the numerical cost of the associated nonlinear simulations is a strong counterpart that designers and engineers are not always prone to pay for. In addition, no model is precise enough to account for every single dissipation phenomenon occurring in a RC structure during a seismic loading.

For these reasons, the common practice is to consider a simpler structural model associated to an additional viscous damping to account for the dissipations not explicitly modeled. Especially, energy dissipation appears even in the linear domain of the material behaviors [12]. The origins of these dissipations may be multiple: soil-structure interaction, nonstructural elements dissipation, friction in joints, friction, etc. Rayleigh-based damping models – including Caughey's series [8] – are convenient and popular in the earthquake engineering community since they allow a fuzzy description of these sources through a viscous force field. Classical Rayleigh-damping models come with now well-known drawbacks [29, 30], depending on which version of the model is chosen (mass proportional, initial stiffness proportional, tangent stiffness proportional, or Caughey's series). Additional viscous damping should be considered carefully when used in combination with a hysteretic model as emphasized in [9, 21]. Indeed, the viscous contribution should be reduced progressively once in the nonlinear domain [12], otherwise the total dissipated energy may be overestimated thus leading to a non-conservative result.

For this reason, the amount of dissipated energy is a strong concern to calibrate whatever the chosen model is. Let us consider a (nonlinear) single degree of freedom (SDOF) oscillator of constant mass m and angular eigenfrequency ω_0 excited by a sinusoidal displacement of angular frequency ω. Jacobsen [27, 28] has shown that a linear viscous damping force of the form of equation (1), where c is the viscous damping coefficient and $\dot{u}$ is the oscillator velocity, is able to represent with an acceptable accuracy the dissipations of a more general nonlinear viscous damping force.

$$F_d(t) = -c \cdot \dot{u}(t) \tag{1}$$

His method can be graphically summarized on figure 1 for a

*Corresponding author
**Principal corresponding author
Email addresses: thomas.heitz@lmt.ens-cachan.fr (T. Heitz), alain.lemaoult@cea.fr (A. Le Maoult), benjamin.richard@cea.fr (B. Richard), cedric.giry@lmt.ens-cachan.fr (C. Giry), frederic.ragueneau@lmt.ens-cachan.fr (F. Ragueneau)

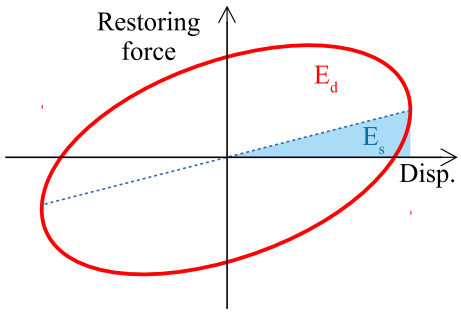

Figure 1: Principle of Jacobsen's areas method [28] applied on a linear viscous SDOF oscillator response

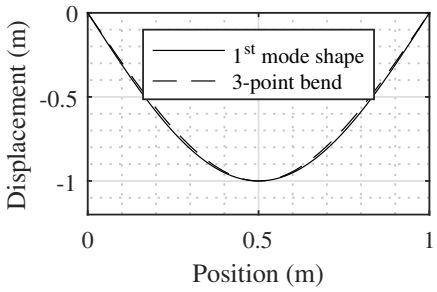

(a) Deformed shape comparison for 3PB versus first mode shape

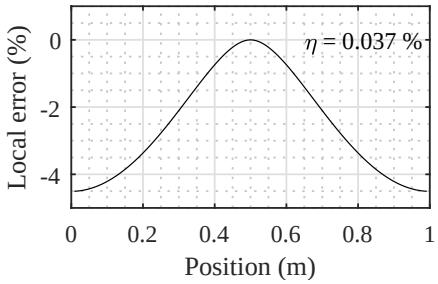

(b) Local error $e(x)$ between 3PB and first mode shape

Figure 2: Comparison between 3-point bend deformed shape and first mode shape of the beam

linear viscous SDOF oscillator response. The restoring force *versus* displacement plot allows for a quick estimation of both the energy dissipated during one oscillation E_d, corresponding to the area enclosed in the red curve, and the maximum energy stored energy during this cycle E_s corresponding to the area under the straight line between the origin and the the point of maximum displacement (since the oscillator is linear). Then, the equivalent viscous damping damping ratio (EVDR) defined as the ratio of the actual damping coefficient c over the so-called critical damping $c_c = 2 \cdot m \cdot \omega_0$ corresponding to the damping coefficient below which oscillations exist if the SDOF is relieved from an out-of-equilibrium state. Then the following equations arise:

$$\xi = \frac{c}{c_c} = \frac{c}{2 \cdot m \cdot \omega_0} \tag{2}$$

and

$$\xi = \frac{1}{4 \cdot \pi} \cdot \frac{\omega_0}{\omega} \cdot \frac{E_d}{E_s} \tag{3}$$

equation (3) being the one proposed by Jacobsen [28] and further discussed for nonlinear cases in section 4.3. Basically, the EVDR can be seen as proportional to the ratio of energy dissipated during one cycle over the energy storage capacity of the SDOF.

This method stays reliable up to a certain extent whether viscous [1] or nonviscous phenomena are involved [2]. Consequently, a N-degrees of freedom oscillator would require N equivalent viscous damping coefficients. From this point arises challenging problems regarding the equivalent viscous damping coefficients values associated to each eigenmode, their evolution throughout the inelastic time history analysis, and the possible existing couplings between modal dampings.

Two goals have driven the development of the experimental campaign in order to address the aforementioned issues:

- it should allow for a mode-per-mode as well as mode-coupled dissipations identification;
- the tests must be driven by the degradation level in order to identify the influence of this parameter on energy dissipations. The sensitivity studies regarding other parameters such as material properties should not be corrupted by an uncontrolled evolution of the structural state.

This paper will firstly give an overview of existing experimental campaigns. This will then help to introduce the experimental campaign design for this work. Finally, the relevance of the design is supported by the presentation of noticeable post-treated results.

2. An overview of experimental campaigns

2.1. Quasi-static tests

Quasi-static tests are generally easier to setup, and allow for canceling inertial effects that are inherent to seismic loadings. This characteristic makes them more convenient to identify dissipations which are independent on the velocity or on the acceleration, since both are negligible. However, there is an information loss regarding the dependency of the damping on the excitation frequency. According to Jacobsen [28], the approximation of structural damping by an equivalent viscous damping (i.e. proportional to the velocity) is realistic enough for structures exhibiting light to moderate nonlinear phenomena. In fact, the EVDR ξ_{eq} identified by Jacobsen's method dissipates the right amount of energy when the SDOF system is excited exclusively at the associated eigenfrequency and when loops in the force-displacement curve are complete.

The tests carried out by Crambuer [13] on RC beams subjected to quasi-static cyclic reverse three-point bend (3PB) loadings aimed to evaluate the EVDR for different damage levels and cycle amplitudes (force-controlled). The underlying hypothesis is that the recorded quasi-static response is the one of the associated SDOF in dynamics. However, because of inertial effects, the flexural mode shape of the beam is sinusoidal while the deformed shape during the 3PB test is a third degree polynomial function. This observation challenges the validity of the aforementioned hypothesis, but the difference remains

Table 1: Overview of damping models based on ductility level in the literature

Authors	Expression of ξ	Remarks
Rosenblueth et Herrera, 1964 [46]	$\xi_0 + \frac{2}{\pi} \cdot \left[\frac{(1-r)\cdot(\mu-1)}{\mu - r\cdot\mu + r\cdot\mu^2}\right]$ (6)	For unspecified flexible elements
Gulkan et Sozen, 1974 [20]	$\xi_0 + 0.2 \cdot \left(1 - \frac{1}{\sqrt{\mu}}\right)$ (7)	Based on Takeda model, for RC frames
Iwan, 1980 [26]	$\xi_0 + 0.0587 \cdot (\mu - 1)^{0.371}$ (8)	For elastic and Coulomb slip elements
Kowalsky, 1994 [31]	$\xi_0 + \frac{1}{\pi} \cdot \left(1 - \frac{1-r}{\sqrt{\mu}} - r \cdot \sqrt{\mu}\right)$ (9)	Based on Takeda model with $\alpha = 0.5$ and $\beta = 0$
Priestley, 2003 [39]	$\xi_0 + \frac{1.50}{\mu\cdot\pi} \cdot (\mu - 1)$ (10)	For steel members
Priestley, 2003 [39]	$\xi_0 + \frac{1.20}{\pi} \cdot \left(1 - \frac{1}{\sqrt{\mu}}\right)$ (11)	For concrete frames
Priestley, 2003 [39]	$\xi_0 + \frac{0.95}{\pi} \cdot \left(1 - \frac{1}{\sqrt{\mu}}\right)$ (12)	For concrete columns and walls
Priestley, 2003 [39]	$\xi_0 + \frac{0.25}{\pi} \cdot \left(1 - \frac{1}{\sqrt{\mu}}\right)$ (13)	For precast walls or frames with unbonded prestressing
Elmenshawi et Brown, 2009 [18]	$\xi_0 + 0.061 \cdot \ln\mu$ (14)	
Rodrigues *et al.*, 2011a [45]	$\xi_0 + 0.0518 \cdot \ln\mu$ (15)	For RC columns
Rodrigues *et al.*, 2011b [45]	$0.2725 - \frac{0.2225}{\mu^{0.37}}$ (16)	For RC columns

small as shown in figure 2. The local error criterion used in figure 2b is defined in equation (4), with x the position along the beam, u the 3PB deformed shape normalized by the mid-span displacement and ϕ_1 the first mode shape also normalized by its mid-span value. The global error criterion expressed in equation (5) (with L the beam span) indicates the good accordance of the 3PB deformed shape with the first mode shape.

$$e(x) = \frac{u(x) - \phi_1(x)}{\Phi_1(x)} \tag{4}$$

$$\eta = \frac{\int_0^L |u(x) - \phi_1(x)| \cdot dx}{\int_0^L |\phi_1(x)| \cdot dx} \tag{5}$$

Another experimental campaign consisting in quasi-static tests has been carried out by Rodrigues et al. [45] and focused on the assessment of dissipations in cantilever RC columns under biaxial cyclic loadings in both directions of the transverse plane. Several RC sections, reinforcement patterns and loading trajectory have been studied. The energy dissipated per cycle, the cumulative dissipated energy and the hysteretic damping ratio have been investigated (the latter being deduced from the two former by Jacobsen's equivalence, recalled in section 4.3 with equation (3)). Finally, two simplified expressions allowing a rough estimation of the so-called biaxial damping in RC columns are proposed (equations (15) and (16)).

It is interesting to mention another study carried out by [18] on RC beam-column connections which leads to a damping ratio evolution law having the exact same form as equation (14). However, Rodrigues et al. [45] state that these expressions should be corrected on the basis of nonlinear time-history analysis and dynamic shaking table tests.

Almost every equivalent damping ratio model listed in table 1 and plotted on figure 3 increases with respect to the displacement ductility factor $\mu = \frac{\delta_{max}}{\delta_y}$ with δ_{max} the maximum observed displacement and δ_y the steel yielding displacement. The two exceptions are Rosenblueth et Herrera [46] and Priestley [39] which show a decreasing EVDR beyond a certain value of ductility due to the post-yielding stiffness coefficient r. When the latter is set to zero, the EVDR is monotonically increasing as with the other models. However, those models do not take into account the influence of the displacement amplitude, which represent an interesting effect to study.

2.2. *Free vibration tests*

The principle of this test is to bring a SDOF structure away from its equilibrium state at a prescribed displacement (e.g. with an actuator), and to release it as suddenly as possible (generally without initial speed) in order to record the decay envelope of the oscillations. A common method to evaluate an EVDR through this test is to apply the logarithmic decrement method (LDM) as illustrated on figure 4.

The main question is: how to address a nonlinear damping since the associated decay envelope does not follow an exponential law? An equivalent viscous damping can be formulated considering that an exponential envelope is a good approximation only between two successive maxima. Hence, EVDR has to be evaluated several times and a mean value could be finally considered, keeping in mind that EVDR could also depend on the amplitude of the oscillations which varies during the test. A somehow equivalent method is proposed by Salzmann et al. [3] and consists in finding the best fitting straight line through the plot of the natural logarithm of oscillation peaks.

This type of test is difficult to execute because it requires a good knowledge of the initial conditions (position, velocity, acceleration). Carneiro et al. [7] tackle this challenge thanks to pseudo-dynamic tests allowing for a quasi-static experimental loading applied by an actuator at the tip of a RC beam deduced from a numerical dynamic simulation.

2.3. *Low level dynamic excitations*

Hammer shock tests are widely used among the researchers and engineers communities [38, 5, 6, 19]. The two main advantages are that (i) they are easy to perform since they only require the dedicated hammer and at least one accelerometer, a measure only takes few seconds, and (ii) they are not destructive and repeatable at will. The latter point counterbalances the fact that, according to Reynolds and Pavic [41], 10 to 20 % of the shocks are spoiled by a rattling phenomenon. However, the same authors found out that shaker excitation allows for higher quality measurements than hammer tests thanks to a more favorable signal-to-noise ratio. A similar study conducted by Ndambi et al. [36] shows that nonlinearities still have a major influence on the scatter of damping ratios, whatever is the technique used.

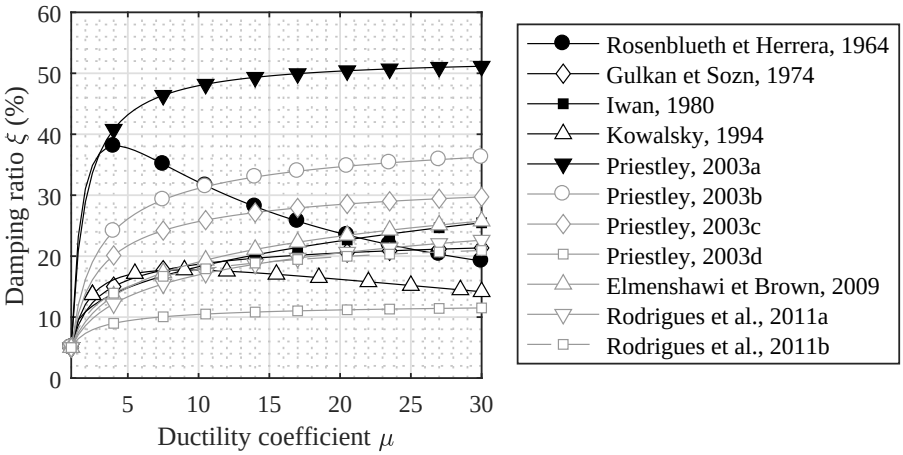

Figure 3: Comparison plot of models for RC beams expressed in table 1 with ξ_0 = 5 % and r = 0.05

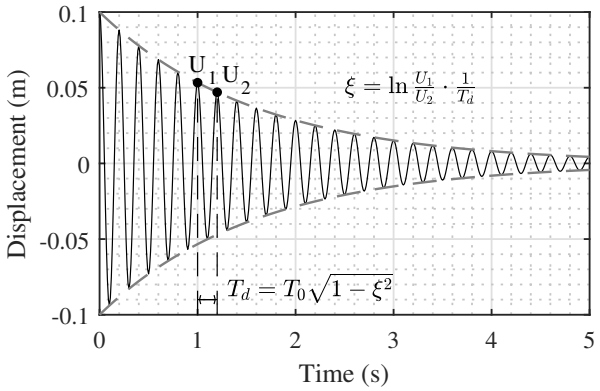

Figure 4: Logarithmic decrement method (LDM), T_0 is the natural period of the undamped oscillations

Ambient seismic noise monitoring are mostly used on existing structures [36, 16]. Some of them rely on the random decrement method initially developed by [10], or also on the frequency decomposition domain method (FDD) [35]. The result is a low amplitude free regime oscillation which has to be treated as described in section 2.2. Those ambient seismic noise records can also be post-treated by the so-called half bandwidth method (the reader will refer to [4] for a literature review of the method and an incertitude propagation study). The methods associated to ambient seismic noise generally require longer recording time than other methods presented in this article to counterbalance the unfavorable signal-to-noise ratio.

2.4. High level dynamic excitations

Hydraulic jacks are commonly used as actuators for high level dynamic excitation. For economical or technical reasons, not all experimental facilities can afford a shaking table. When available, it is probably the best suited piece of equipment for studying complex structures such as for SMART 2008 [43] or SMART 2013 [42] international benchmarks on a scaled two-story RC building. The control quality is of first importance in this case, because the structure itself may disturb the actuators because of inertial effects. More reasonable setups can also provide rich information such as electromagnetic or mechanical shakers [15], mostly when simple SDOF-like structures of moderate size are studied. The main challenge concerns the damping evaluation during those tests because of the many phenomena involved and the evolution of the sought properties during the loading: this motivates the choice of tests at the component scale. For this reason, consolidating intermediate low level dynamic tests are performed during the experimental campaign.

3. Experimental campaign

3.1. Framework

In the framework of SINAPS@ project [25], the IDEFIX experimental campaign took place in the TAMARIS experimental facility at the French Alternative Energies and Atomic Energy Comission (CEA) from May to November 2016. Twenty RC beams have been casted and their dimensions have been designed in order to make their first two eigenmodes being in the optimally-controlled frequency range of the shaking table, *Azalée*, i.e. under 30 Hz according to IDEFIX boarded mass. The experimental protocol ensures the acquisition of relevant data to estimate degradations and energy dissipations in and at the boundaries of the structure.

On the basis of the literature review of experimental campaigns dedicated to the study of energy dissipations in RC components in section 2, the choice has been made to design a campaign that includes the main types of loadings (quasi-static, low and high level dynamic) performed on elements that are more simply modeled than others, i.e. beams. Ambient seismic noise based methods require long duration recording to counterbalance the poor signal-to-noise ratio. For this reason, the authors have decided not to use them.

3.2. Specimens

The specimens are six-meter long RC beams with a cross-section of 20 cm × 40 cm. Two concrete classes, two steel reinforcements types and three different diameters are chosen to design a total of six designs of specimens listed in table 2. A typical beam weights around 1150 kg. For the sake of clarity,

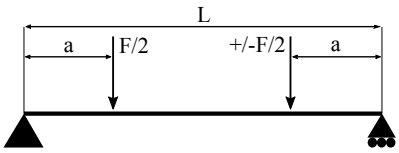

Figure 5: Configuration of the quasi-static tests, with $L = 5.9$ m and $a = \frac{L}{4}$

each beam has been labeled with respect to its characteristics (i.e. type of reinforcement and concrete):

- The two steel reinforcements types are ribbed B500B steel bars following European standards (norm BS 4449, conforming to the Eurocode 2 [11]) labeled HA (standing for "high adherence") and round steel bars labeled RL. The three different diameters are 12 mm, 16 mm and 20 mm. The reinforcement patterns are described in table 2 and will be later labeled in a shorter way (respectively): HA12, RL12, HA16 and HA20. The reinforcement ratios of 10HA12, 10RL12 and 4HA20 are close while the one of 8HA16 is higher. Similarly, 10HA12, 10RL12 and 8HA16 have a close interface surface (i.e. surface of the steel-concrete bond, idealized as a cylinder with a diameter equal to the nominal diameter of the reinforcement) while the one of 4HA20 is lower.
- Two concrete classes have been formulated, they correspond to C25/30 and C45/55 classes as defined in Eurocode 2 section 3.1.2 [11] and are labeled respectively C1 and C2 for this campaign. Two casts were necessary for the concrete C1 and they proved to have different mechanical properties. This motivates the choice to distinguish two variants of C1, namely C1A and C1B.

3.3. *Strong floor tests*

Eight beams have been tested on a strong floor in a four-point bend configuration (figure 5) with two hydraulic cylinders of 25 kN capacity each, a maximum velocity of 1.6 m·s^{-1}and a maximum displacement of ±120 mm. The choice of a 4PB test is made in order to better approximate the first two modes shapes thanks to the actuators (more details are given regarding this point in section 3.7.1).

3.4. *Shaking table tests*

The twelve other beams have been tested on *Azalée* shaking table which measures 6 m × 6 m. The particularity of this equipment is its ability to move in three translations and three rotations.

3.5. *Boundary conditions and additional masses*

The beam-end supports consist in elastic "blades" (figure 7b) mounted in parallel in order to free the rotation of the beam around the vertical axis without inducing spurious friction mechanisms. High-performance steel (Marval 18H®, yield stress $R_{p,0.2\%}$ = 1860 MPa and Young's modulus E = 186 GPa) has been used and allows the thinnest part of these blades for being

Table 2: Different beam designs

Label	HA20-C1A	HA16-C1A	HA12-C1A
Pattern design		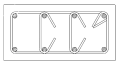	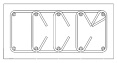
Pattern label	4HA20	8HA16	4HA12
$\rho^{(1)}$ (%)	1.57	2.01	1.41
$S_b{}^{(1)}$ (cm^2·m^{-1})	25.1	40.2	37.7
Steel label	HA20	HA16	HA12
$f_s{}^{(1)}$ (MPa)	>560$^{(2)}$	568	528
$E_s{}^{(1)}$ (GPa)	237	217	206
Concrete label	C1A	C1A	C1A
Concrete class	C25/30	C25/30	C25/30
$f_{c,28d}{}^{(1)}$ (MPa)	35.0	35.0	35.0
$f_{c,6m}{}^{(1)}$ (MPa)	36.9	36.9	36.9
$E_{c,28d}{}^{(1)}$ (GPa)	26.4	26.4	26.4
$E_{c,6m}{}^{(1)}$ (GPa)	26.2	26.2	26.2

Label	HA12-C1B	RL12-C1B	HA12-C2
Pattern design	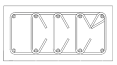	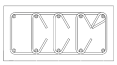	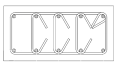
Pattern label	4HA12	4RL12	4HA12
$\rho^{(1)}$ (%)	1.41	1.41	1.41
$S_b{}^{(1)}$ (cm^2·m^{-1})	37.7	37.7	37.7
Steel label	HA12	RL12	HA12
$f_s{}^{(1)}$ (MPa)	528	468	528
$E_s{}^{(1)}$ (GPa)	206	218	206
Concrete label	C1B	C1B	C2
Concrete class	C25/30	C25/30	C45/55
$f_{c,28d}{}^{(1)}$ (MPa)	29.7	29.7	45.4
$f_{c,6m}{}^{(1)}$ (MPa)	33.0	33.0	47.4
$E_{c,28d}{}^{(1)}$ (GPa)	28.7	28.7	29.2
$E_{c,6m}{}^{(1)}$ (GPa)	28.1	28.1	28.2

(1) ρ: reinforcement ratio – S_b: interface surface – f_y: steel yield stress – E_s: steel Young's modulus – $f_{c,28d}$: concrete strength at 28 days – $f_{c,6m}$: concrete strength at 6 months – $E_{c,28d}$: Concrete Young's modulus at 28 days – $E_{c,6m}$: Concrete Young's modulus at 6 months.
(2) Maximum force capacity of the testing machine reached

(a) Setup on strong floor

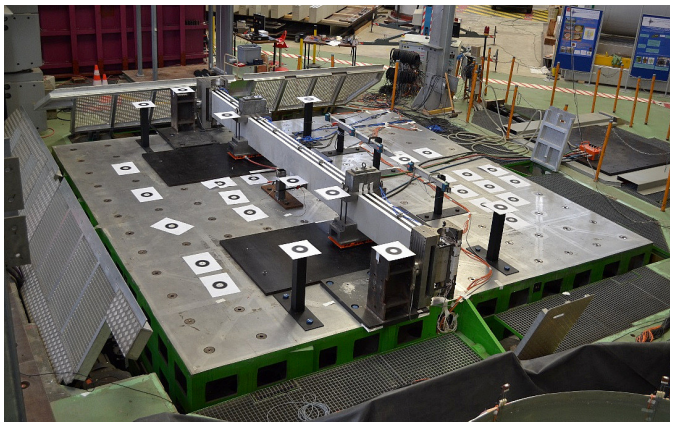

(b) Setup on *Azalée*

Figure 6: IDEFIX experimental setup on the strong floor (a) and on the shaking table (b)

only 2.5 mm thick. Another originality regarding the boundary conditions is the use of air cushions at both quarter-spans in order to bear the whole weight of the setup while drastically reducing the friction with the floor. Additional masses of 350 kg are also mounted on the air cushions to fulfill the requirements regarding the first two eigenfrequencies (see section 3.1).

3.6. Measurements

A variety of sensors is used to build a strong database for each test:

- 5 displacement wire sensors;
- an industrial digital image correlation tool (Videometric®, [48]) to track the mid-plane of the beam along the tests;
- 5 gyrometers (to measure the rotational velocity);
- 19 accelerometers;
- 2 six-axis load cells at the beam supports;
- 2 monoaxial load cells on cyclinders.

The sensors setup is described in both figures 7a and 8. Nine reference positions which divide the beam in eight equal parts. Then, each sensor is labeled with respect to its position number (from 1 to 9). The black stripes painted on the upper surface of the beam are tracked by the digital image correlation (DIC) tool which provides a discretized full field measurement of the beam's mid-plane transverse displacement $u(t_j, x_k)$ at time $t_{j\in[\![1,N_t]\!]}$ and at position $x_{k\in[\![1,N_x]\!]}$, $x_{N_x} = L$ being the span of the beam. The linear combination v of the $N_m{}^{\text{th}}$ first flexural mode shapes, which best approximates the measured one u, is sought:

$$v(t,x) = \sum_{i}^{N_m} a_i(t) \cdot f_i(x) \tag{17}$$

where the f_i are the flexural mode shapes and the a_i are the modal coordinates. The identification procedure is performed in a two-staged optimization routine (displacement projection and model identification) as diagrammed in figure 9. To project the displacement field of the beam on a wisely chosen displacement basis – the theoretical mode shape basis here – an objective function is defined in an analogous way to what is done in (Integrated) Digital Images Correlation techniques (I-DIC) [24]. Hence, the following $N_m \times N_t$ minimization problems have to be solved, $\forall\{i,j\} \in [\![1,N_m]\!] \times [\![1,N_t]\!]$:

$$\left\{ a_i(t_j), \frac{\partial}{\partial a_i(t_j)} \left[\int_0^L \left(u(t_j,x) - \sum_i^{N_m} a_i(t_j) \cdot f_i(x) \right)^2 \cdot dx \right] = 0 \right\} \tag{18}$$

Then, a linear system is obtained by differentiation, $\forall j \in [\![1,N_t]\!]$,

$$\mathbf{B} \cdot \mathbf{a}(t_j) = \mathbf{b}(t_j), \text{ with } \begin{cases} \mathbf{a}(t_j) = \left\{ a_i(t_j) \right\}_{i\in[\![1,N_m]\!]} \\ \mathbf{B} = \left\{ \int_0^L f_i(x) \cdot f_l(x) \cdot dx \right\}_{\{i,l\}\in[\![1,N_m]\!]^2} \\ \mathbf{b}(t_j) = \left\{ \int_0^L f_l(x) \cdot u(t_j,x) \cdot dx \right\}_{l\in[\![1,N_m]\!]} \end{cases} \tag{19}$$

In practice, the first three eigenmodes allow representing the beam behavior in a satisfactory way and therefore, only three wisely chosen coordinates are sufficient to express the eigenvectors. An SDOF oscillator described by a set of parameters $\{p\}$ (e.g. damping ratio, eigenfrequency, etc.) is considered to best approximate the modal coordinates a_i along the time. Hence, the model identification procedure relies on the minimization of the functional expressed by equation (20):

$$\varepsilon = \sqrt{\frac{\int_0^T \left(c_i^{\{p\}}(t) - a_i(t) \right)^2 \cdot dt}{\int_0^T a_i(t)^2 \cdot dt}} \tag{20}$$

where $c_i^{\{p\}}(t)$ is the model displacement for the best set of parameters $\{p\}$.

3.7. Overview of the loadings

Table 3 shows an overview of the different loadings which have been tested on the beams during the experimental cam-

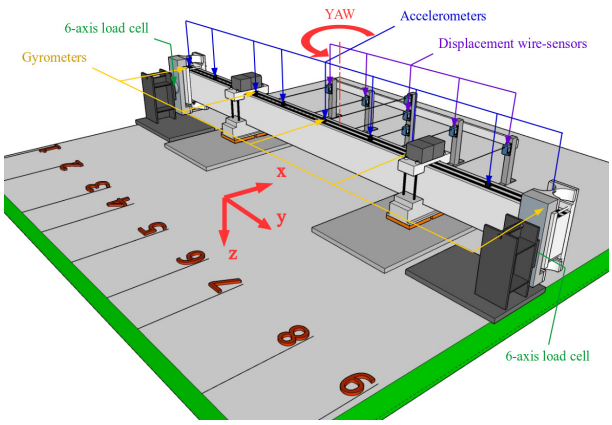

(a) 3D view of the sensors setup and working basis

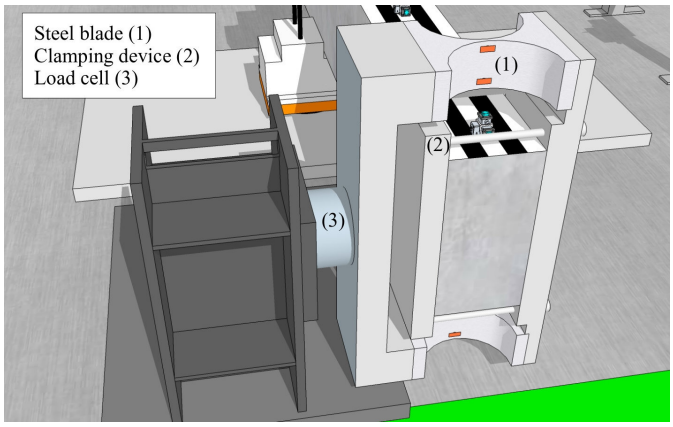

(b) Blades beam supports

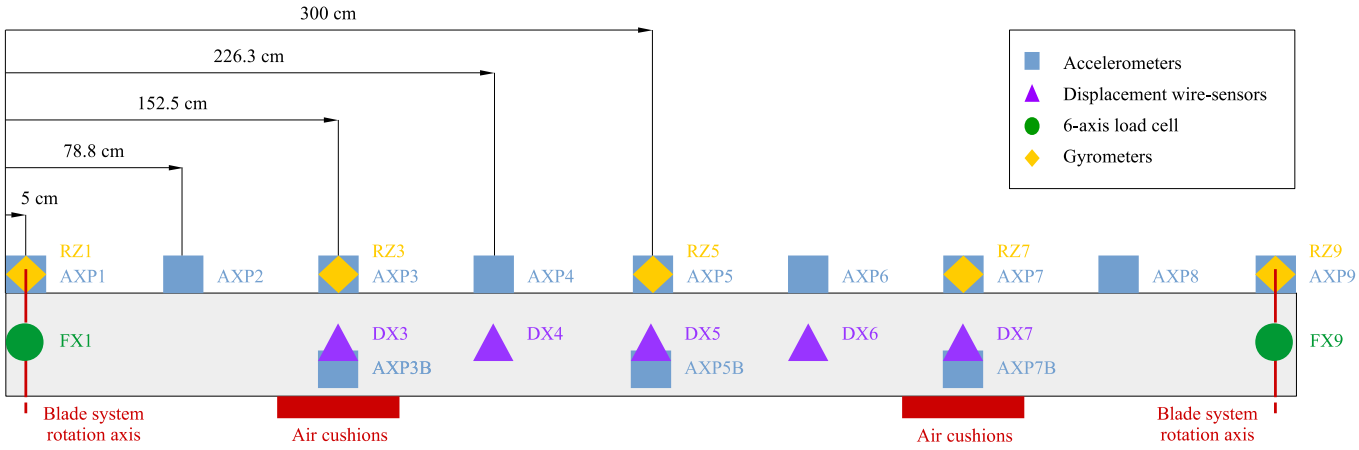

Figure 8: Schematic view of the sensors setup

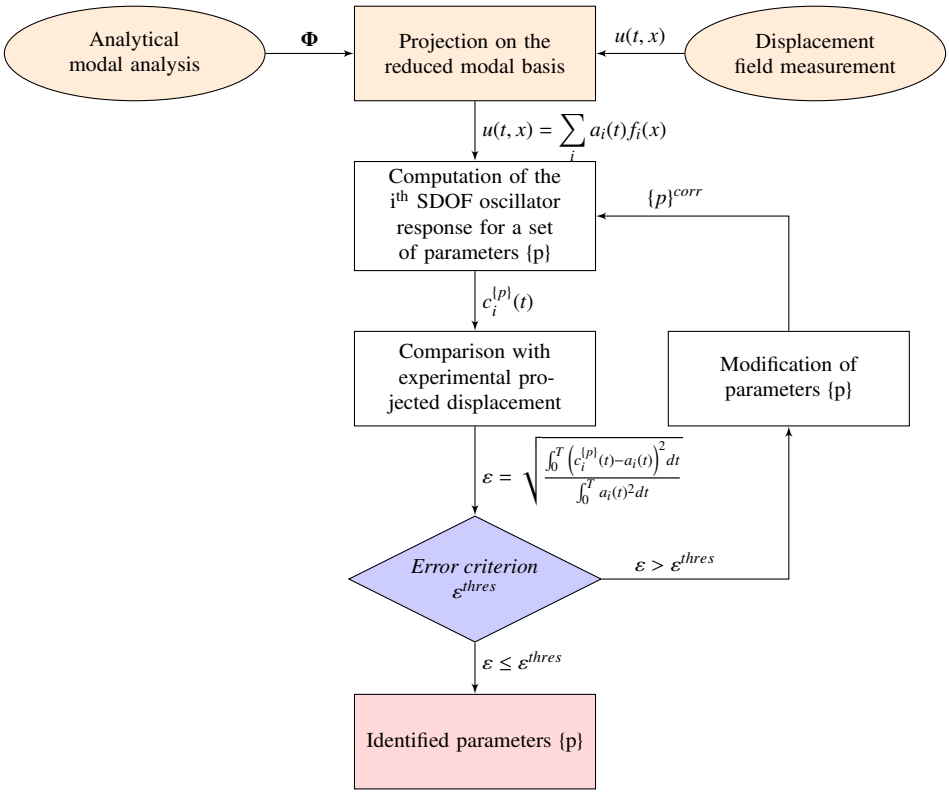

Figure 9: Flowchart of the SDOF identification procedure with support of the DIC measurements

paign.

3.7.1. Quasi-static loadings

There are four different quasi-static loadings. The two firsts, QSC1 and QSC2, are reverse cyclic tests. The displacement amplitude grows by blocks of three cycles as plotted in figure 10, and the loading velocity is 0.4 mm·s^{-1}. The fundamental difference between these two loadings is that the actuators are either in-phase or in phase-opposition. The purpose of these tests is to evaluate the EVDR associated to the first two flexural eigenmodes, that is, QSC2 prescribes a displacement that will create a deformed shape close to the second mode shape of the beam. This is confirmed by figure 11 where the two normalized shapes are compared. The both error indicators show a better agreement between 4-point bend test deformed shape and the 1st mode shape (with additional masses) than the 3-points bending and the 1st mode shape (without additional mass) discussed in section 2.1 (figure 2). Also, the 4-point bending creates an area of constant bending moment in the part of the beam between both actuators. It generates in this area a relatively homogeneous stress/strain state, allowing for reasoning in terms of fracture energy per RC volume. However, it could be argued that 3-point bending would initiate internal friction due to transverse shear forces. For practical (experimental setup), time reason and economical reasons, this participation to the dissipations has not been investigated, but it would represent an interesting addition to IDEFIX experimental campaign.

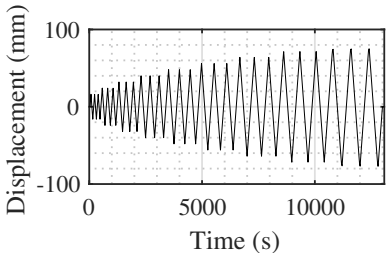

(a) QSC1

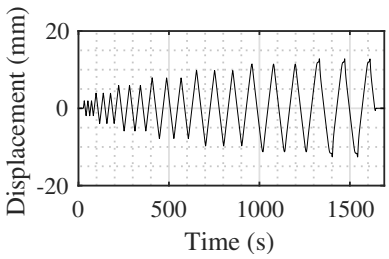

(b) QSC2

Figure 10: Actuator prescribed displacement for QSC1 and QSC2 (at quarter-span)

Table 3: Descriptions of the loadings

Equipment	Reference	Eigenmodes	Description
	HT	1 and 2	Hammer test
	WN1	1	White noise signal in X-direction (duration 200 s)
	WN2	2	White noise signal around YAW-axis (duration 200 s)
	WN3	1 and 2	White noise signal (combination of WN1 and WN2)
	WN1MTS	1	White noise genereted by MTS software
	WND030	1	White noise of table displacement bandpassed between 0 Hz and 30 Hz
	SC1	1	White noise signal in X-direction bandpassed between $0.5 \cdot f_1$ and $1.05 \cdot f_1$, f_1 being the first eigenfrequency
	SC2	2	White noise signal in YAW-direction bandpassed between $0.5 \cdot f_2$ and $1.05 \cdot f_2$, f_2 being the second eigenfrequency
	SC2b	2	White noise signal in YAW-direction bandpassed between $0.35 \cdot f_2$ and $1.05 \cdot f_2$, f_2 being the second eigenfrequency
Azalée	SC12	1 and 2	Combination of SC1 and SC2
	SS1	1	Natural seismic signal, transfered at third floor spectrum of Niigataken-Chuetsu-Oki earthquake (NCOE)
	Sinus	1 or 2	Sinusoidal signal in X-direction or around YAW-axis
	DSS$f_1 f_2$	1 or 2	Harmonic signal at constant amplitude, by decreasing frequency steps (from f_1 to f_2) in X-direction or around YAW-axis
	ISD	1	Step-by-step increasing sinusoidal acceleration following a quadratic law (i.e. a linearly increasing displacement demand)
	BS	1	Continuous linear sinus sweep generated by MTS software
	QSS025	1	Continuous quadratic sinus sweep generated by MTS software
	BiSINUS	1 and 2	Sinusoidal signals consecutively in X, X+YAW and YAW directions
	QSC1	1	Quasi-static reverse cyclic four-point bend test with in-phase actuators
	QSC2	2	Quasi-static reverse cyclic four-point bend test with actuators in phase opposition
Strong floor	SPS1	1	Quasi-static reverse cyclic four-point bend test with in-phase actuators and increasing velocity (constant velocity during one cycle)
	SPS2	2	Quasi-static reverse cyclic four-point bend test with actuators in phase opposition and increasing velocity (constant velocity during one cycle)

3.7.2. Dynamic loadings

Dynamic signals sent on the shaking table command unit are either broad band (white noises, or bandpassed white noises) or harmonic. Advantages are taken from the ability of the table to move simultaneously in two different directions (e.g. along X and/or around YAW for IDEFIX tests). Indeed, the second eigenmode of the beam (i.e. S-shaped mode) is difficult to activate because of the symmetrical construction of the experimental setup. The acceleration on YAW-DOF creates inertial forces in opposite directions on beam and additional masses from each side of table's vertical rotation axis. In order to reach similar levels of excitation for both DOF, an equivalence of absolute acceleration along X-axis at the hinges is chosen. Hence, equation (21) links the rotational acceleration θ_g on YAW-DOF and the acceleration a_g along X-DOF (with L the distance between the two hinges).

$$\theta_g = \frac{2 \cdot a_g}{L} \tag{21}$$

4. Focus on some results

4.1. Capacity curves

4.1.1. Experimental protocol.

The QSC1 tests (figure 10a) performed on the different beam designs allow for computing the capacity curves by considering only the envelope of the force-displacement curves obtained such as pushover analysis. The force considered is the sum of the force measured on each beam support in X-axis, whereas the displacement is measured at mid-span (only the positive

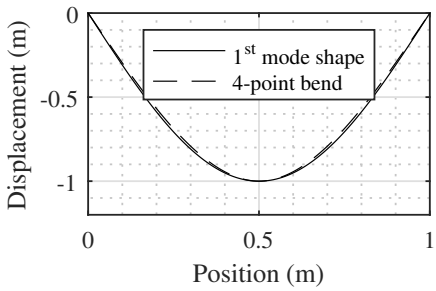

(a) Deformed shape comparison for 4PB versus first mode shape

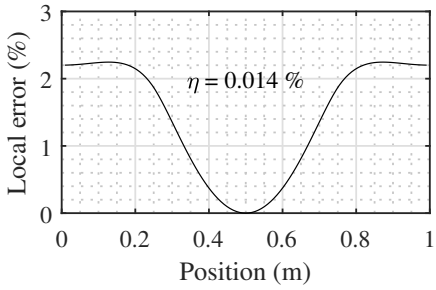

(b) Local and global errors (equations (4) and (5)) between 4PB and 1st mode shape

Figure 11: Comparison between 4-point bend deformed shape and 1st mode shape of the beam taking into account the additional masses

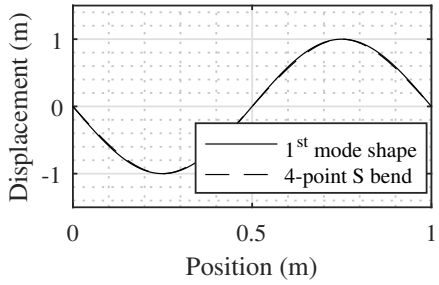

(a) Deformed shape comparison for 4PB versus first mode shape

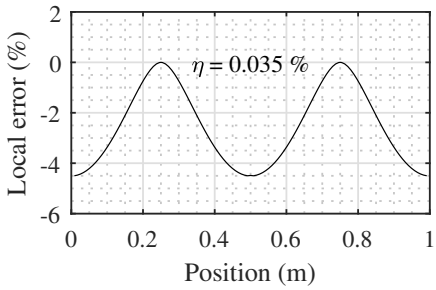

(b) Local and global errors (equations (4) and (5)) between 4-point S bend and 1st mode shape

Figure 12: Comparison between 4-point S bend deformed shape and 2nd mode shape of the beam taking into account the additional masses

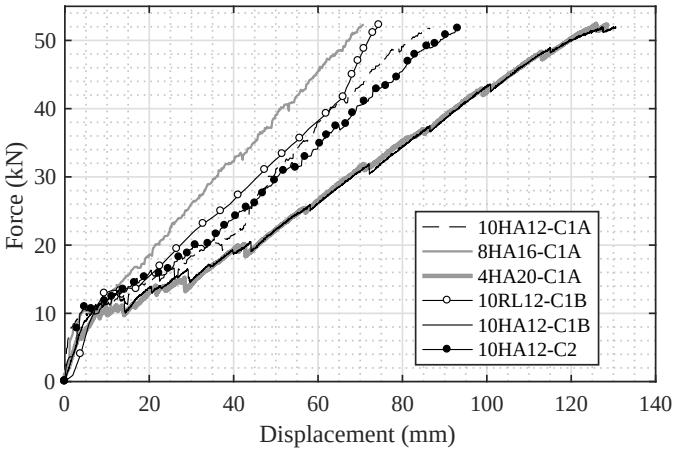

Figure 13: Capacity curves obtained from QSC1 tests

displacements are considered, i.e. when the actuators push on the beam, by convention). These results are plotted in figure 13. For each beam, the nonlinear range begins around 10 kN, with cracks initiation in concrete. In real RC structures, *a fortiori* in nuclear power plants, steel yielding is not expected in beams but rather at structural joints. Hence, the steel yielding is not investigated during this experimental campaign.

4.1.2. Concrete influence.

Beam HA12-C1B exhibits a lower capacity than HA12-C1A because the measured strength for concrete C1A is 36.9 MPa while the one for C1B is 33.0 MPa (10.6 % lower). More surprisingly, the capacity of HA12-C2 is higher than HA12-C1A in the first 50 mm of prescribed displacement, but is then lower. The difference may not be important enough to conclude about the relative capacities of these two variants. Indeed, only one specimen of each could be tested.

4.1.3. Reinforcement pattern influence.

The highest capacity is observed for beam HA16-C1A while the lowest is for beam H20-C1A. The capacity of HA12-C1A is somehow an intermediate between the two previous. These results are in accordance with the specific interface surfaces given in table 2. This may be a more significant indicator of the beam behavior once in the nonlinear range. Indeed, bond slipping occurs at the steel-concrete interface. The higher the interface specific surface is, the higher the friction force between steel and concrete is.

4.1.4. Reinforcement ribs influence.

HA12-C1A has classical high adherence steel reinforcement bars, but RL12-C1A has special reinforcement bars without ribs. The RL12-C1A capacity was expected to be lower than the one of HA12-C1A, but it is finally not the case. A low confinement of the concrete surrounding the reinforcements may explain this results as stated by Daoud et al. [14] when comparing the results of a non-confined pull-out test with both smooth and ribbed bars.

On the contrary in the pull-out tests, a passive confinement due to the experimental setup design described in [44] and pictured in figure 14b increases the bond strength [37]. In figure 14a,

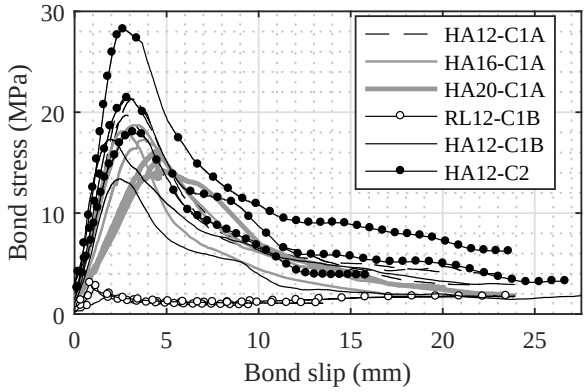

(a) Results of the pull-out tests for different steel-concrete combinations

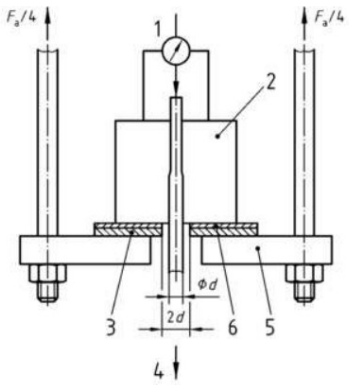

(b) Experimental setup description from [30]

Figure 14: Description and results of the pull-out tests

the so-called "bond stress" is the conventional stress given in equation (22) with the traction force measured during the test, the bar diameter, the target value for the concrete class strength (i.e. 25 MPa for C1A and C1B, and 45 MPa for C2) and the measured mean concrete strength. The results are in good agreement with the one obtained in the work of Eligehausen et al. [17] with a concrete strength of 30 MPa and bar diameters going from 19 mm to 32 mm. Indeed, they get a mean peak value of bond stress of around 14.7 MPa versus 18.2 MPa for IDEFIX, for all diameters and excluding round bars. However, the residual bond stress is lower for IDEFIX pull-out specimens since no transverse reinforcement has been included. The bond stress is:

$$\tau_{dm} = \frac{1}{5\pi}\frac{F_a}{d^2}\frac{f_{cm}}{f_c} \tag{22}$$

with F_a the force pulling the steel bar, d the bar diameter, f_{cm} the measured mean concrete strength and f_c the concrete class strength (i.e. 25 MPa for C1A and C1B and 45 MPA for C2).

4.1.5. Conclusions regarding the capacity curves.

In conclusion, the capacity curves show interesting tendencies:

- no clear link between concrete strength and the capacity curves has been emphasized, maybe due to an insufficient difference between the studied concretes;
- the reinforcement specific surface (steel-concrete interface surface per unit length) increases the post-yield stiffness of the beam;
- the absence of ribs on the reinforcement bars does not influence the capacity curves, probably because of a low confinement.

4.2. Cyclic quasi-static test

A post-treatment of the cyclic quasi-static test QSC1 (figure 10a) performed on the beam HA20C1A1 is presented in this subsection. The force-displacement curve exhibits mainly three phenomena: stiffness loss, hysteresis loops and a pinching effect. The stiffness loss is essentially due to cracking. Hystereses have several origins which are not easy to model neither identify. Anyway, crack surfaces friction and bond slipping are supposed to play a major role in this phenomenon. Finally, the so-called pinching effect consists in a stiffness reduction in the neighborhood of the zero-displacement point that explains the reversed S-shape of the load displacement curve in figure 15. This effect is still not entirely understood.

Thanks to the digital image correlation (DIC) device described in section 3.6, it is possible to make a projection of the measured transverse displacement field $u(t, x)$, on the theoretical eigenbasis $\mathbf{\Phi}$. The resulting error is plotted in figure 16 against the position on the beam and the time. Maximums appear at the beam tips (maximum absolute error about 3 mm in this case) due to the presence of the mounting system masking the stripes pattern tracked on the beam. This effect remains local and does not seem to disturb the global projection error since

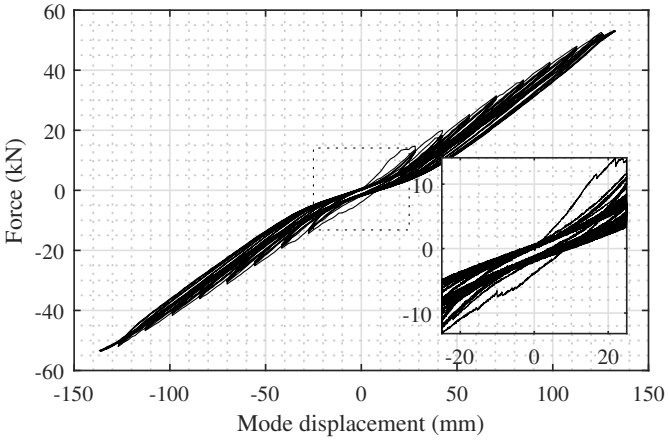

Figure 15: Force-displacement curve obtained after QSC1 test performed on beam HA20-C1A-1

it stays otherwise as low as a mean absolute value of 0.16 mm for the discretization used in this case (i.e. 201 points distant of 29.5 mm).

4.3. Damping identification from cyclic reverse quasi-static tests

Jacobsen [28] developed the concept of equivalent viscous damping ratio as the damping ratio of a linear dashpot that would dissipate the desired amount of energy at the associated SDOF's eigenfrequency. To this end, the equivalent viscous damping ratio is evaluated by the ratio of the energy dissipated per cycle over the elastically stored energy per cycle in equation (3). It is interesting to mention that the term $\frac{\omega_0}{\omega}$ is often omitted, meaning that the equivalent linear oscillator has to oscillate at its eigenfrequency to dissipate the correct amount of energy (i.e. compared with the reference nonlinear oscillator), which strongly reduces the applicability range of Jacobsen's formula. Therefore, it is important to keep in mind that the EVDR obtained thanks to Jacobsen's method are generally given for an oscillation at $\omega = \omega_0$ and has to be adapted for different frequencies.

The classical Jacobsen's areas method was originally developed to evaluate the EVDR for nonlinear frictional system. Two points remain questionable:

- the stored linear elastic energy is generally supposed to be square-proportional to the displacement (figure 17a) but this hypothesis is inexact in the case of a nonlinear behavior which is the case when pinching occurs for example (figure 17b);
- when the loops are not symmetric, there is no actual reason to pick up the maximum relative displacement rather than the minimum one when assessing the stored elastic energy. For this reason, [32] proposed an approach adapted to asymmetric hysteretic behaviors. As depicted in figure 17c. A method inspired from this work and more suitable for nonlinear restoring forces is proposed in figure 17d.

The energy dissipated during the cracking initiation and propagation should not be included in the EVDR evaluation since it induces unrealistic damping ratio values. This explains why every three cycles, a leap of damping ratio is observed in figure 18. When going to the next loading block of the cycles of the same amplitude (figure 10a), the damage state of the beam increases, dissipating a large amount of energy for the first cycle. For this reason, only the third cycle of each block is used to apply Jacobsen's areas method. The elastic limit has been here identified at 5.2 mm.

Second degree polynomial functions of the displacement amplitude fit very well both stored and dissipated energy per cycle (figure 19). As a direct consequence of equation (3), an inverse function of the form $y = a + b \cdot x^{-1}$ describes the evolution of the EVDR against the displacement amplitude (figure 20). This result is in agreement with the several authors [47, 33, 34] who studied the response of slender buildings under dynamic loads and contradicts the hypothesis of a linear viscous damping. Among expressions proposed by [45, 40, 31] only Kowalsky's [31] (equation (9)) allows for a decreasing EVDR. Despite the fact that experimental data do not give information regarding ductility coefficient values lower than 4, the EVDR is expected to increase in the first place until a maximum is reached. This hypothesis has been studied in [22] through numerical simulations performed on a hysteretic model calibrated on experimental data. It is shown in the same study that the EVDR not only depends on the ductility coefficient but also on the current cycle amplitude of displacement itself. In other words, an hysteretic model at a given ductility level μ_1 associated to a maximum historic displacement δ_m and submitted to a cyclic prescribed displacement of amplitude δ, the EVDR value depends on both μ_1 and δ. In an ideal case, all the progressive loading procedure should be carried out at each degradation level (from zero to the current degradation state) in order to uncouple the both influences. This aspect has been investigated in the aforementioned paper [22].

4.4. White noise on shaking table

Among the dynamic tests, a focus is made in this paper on the white noise signal labeled WN12 sent on *Azalée* shaking table on both X and YAW-DOF. The loading procedure is detailed in table 4 in which the so-called damage level refers to the highest peak ground acceleration (PGA) experienced by the beam in its time-history. Beforehand, the beam is excited by a white noise signal at the reference PGA and then excited by increasing white noise signals for lower PGA (prescribed PGA along X-axis around 0.19 g, 0.20 g, 0.23 g, 0.26 g, 0.31 g, 0.34 g and 0.41 g). The rule of equation (21) aforementioned in section 3.7.2 is here not strictly followed because of the imperfect online control of the shaking table.

A preliminary hammer shock test allows for an accurate estimation of the experimental setup's eigenfrequencies (7.14 Hz for the first eigenmode and 22.9 Hz for the second one) and a first estimation of the EVDR thanks to the half-bandwidth method. The frequency response function (FRF) has been obtained thanks to the accelerometer grid (figure 22). In comparison, the same method is applied on a low level WN12 (run 516) and gives the plain black line in the power spectrum density (PSD) versus frequency plot in figure 23. The results of both hammer tests and low-level white noise are summarized in table 5. This shows

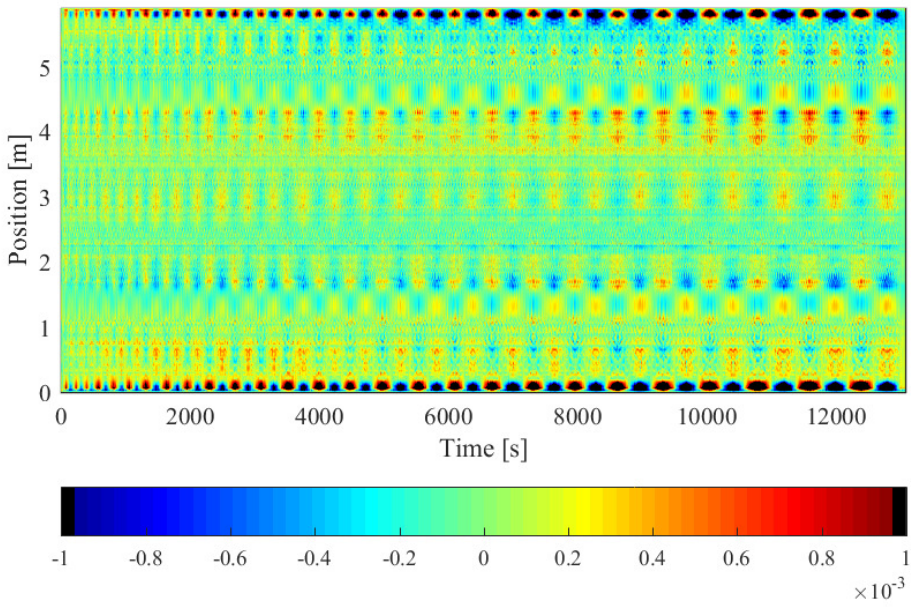

Figure 16: Spatiotemporal error map after projection on modal basis for QSC1 test (error in meters)

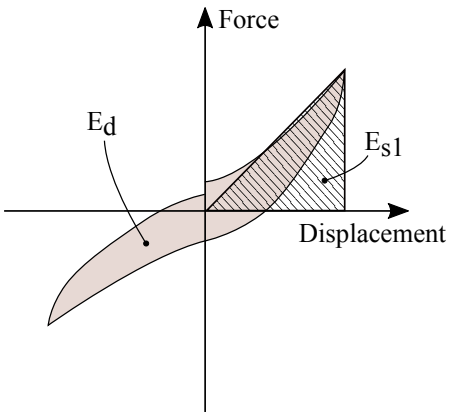

(a) Linearly stored energy evaluated on a half-cycle

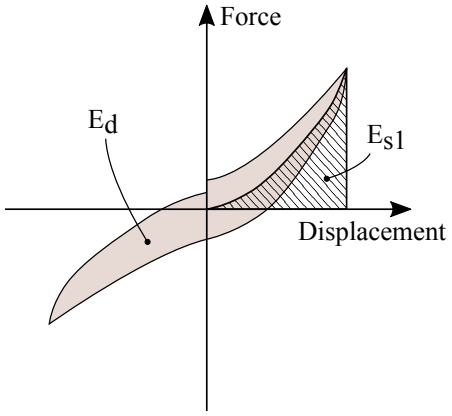

(b) Nonlinearly stored energy evaluated on a half-cycle

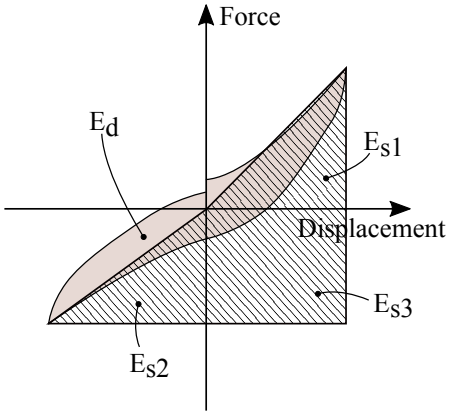

(c) Linearly stored energy evaluated on a full-cycle by Kumar et al. [32]

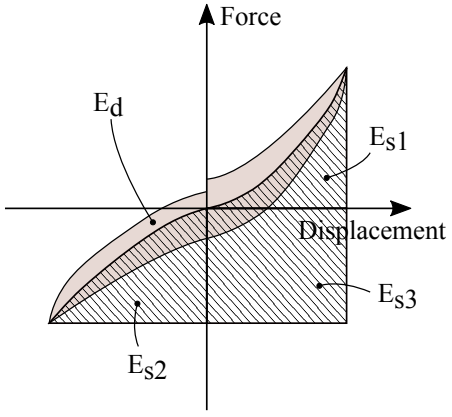

(d) Nonlinearly stored energy evaluated on a full-cycle inspired by Kumar et al. [32]

Figure 17: Different ways to apply areas method derived from Jacobsen [28] and Kumar et al. [32]

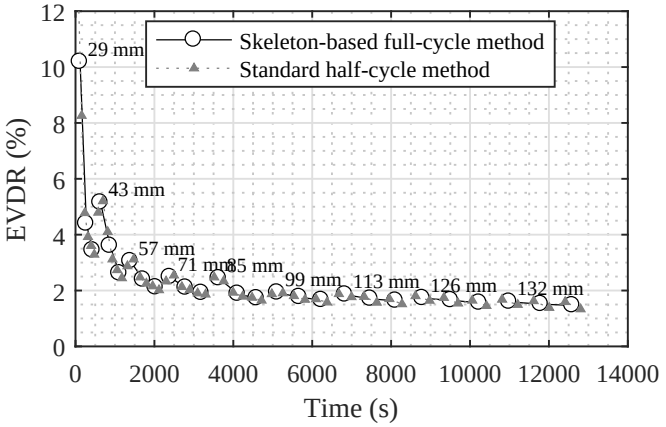

Figure 18: EVDR values deduced from Jacobsen's areas method along time-history analysis (for methods illustrated on figures 17a and 17d)

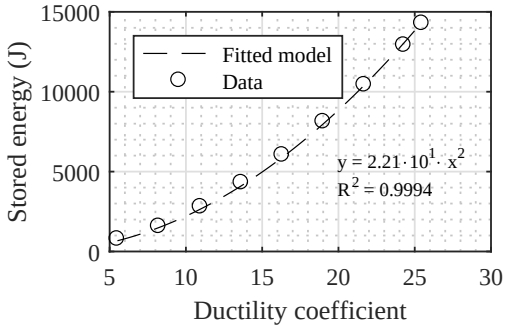

(a) Stored energy per cycle

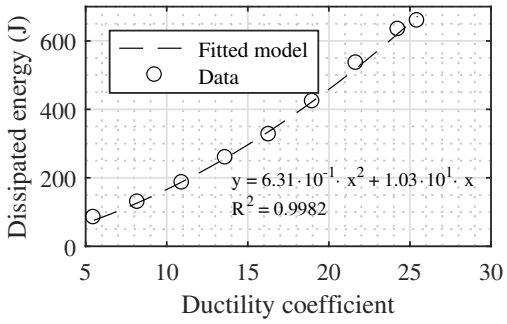

(b) Dissipated energy per cycle

Figure 19: Energies engaged during QSC1 tests

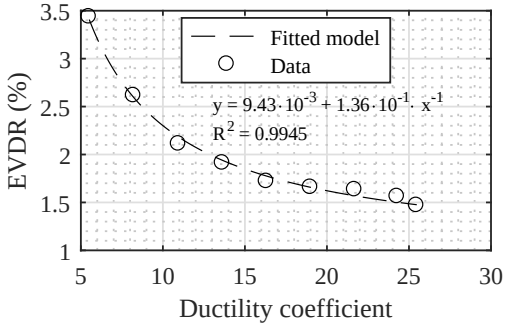

Figure 20: EVDR values deduced from Jacobsen's areas method

Table 4: Loading procedure followed for WN12 tests

Damage level	1	2	3	4	5	6	7
RUN	516	518	520	523	527	532	538
PGA X (g)	0.17	0.18	0.17	0.18	0.19	0.18	0.27
PGA YAW (°·s^{-2})	37.8	36.3	35.7	32.8	34.3	33.7	39.3
RUN		517	521	524	528	533	539
PGA X (g)		0.21	0.23	0.22	0.22	0.18	0.18
PGA YAW (°·s^{-2})		50.9	47.9	48.8	49.4	51.1	52.8
RUN			519	525	529	534	540
PGA X (g)			0.24	0.25	0.28	0.21	0.19
PGA YAW (°·s^{-2})			64.3	69.9	66.7	62.1	75.7
RUN				522	530	535	541
PGA X (g)				0.25	0.27	0.27	0.24
PGA YAW (°·s^{-2})				90.8	86.7	83.4	103.4
RUN					526	536	542
PGA X (g)					0.32	0.33	0.28
PGA YAW (°·s^{-2})					112.3	104.3	120.6
RUN						531	543
PGA X (g)						0.34	0.33
PGA YAW (°·s^{-2})						122.9	124.6
RUN							537
PGA X (g)							0.41
PGA YAW (°·s^{-2})							147.1

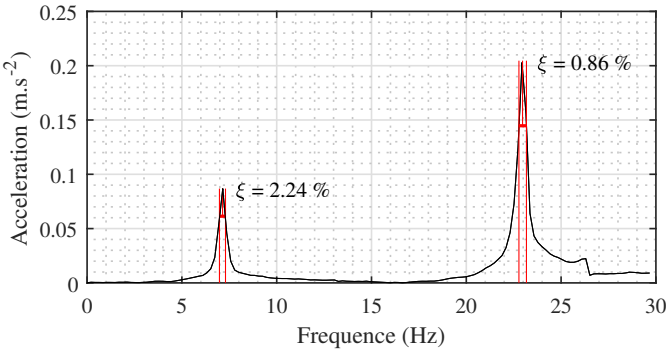

Figure 21: Half-power bandwidth method applied on hammer shock test performed prior to WN12

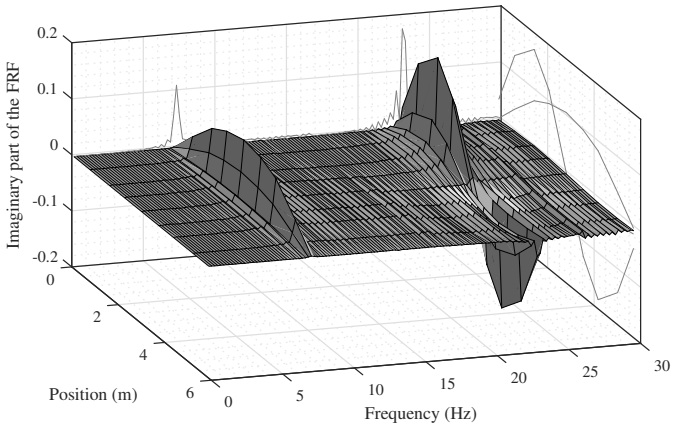

Figure 22: Hammer shock test post-treatment

Table 5: Modal analysis results for low-level dynamic signals on beam HA20-C1A-2

Estimate	f_1 (Hz)	f_2 (Hz)	ξ_1 (%)	x_2 (%)
Hammer test	7.14	22.9	2.24	0.86
White noise	7.13	22.5	2.51	0.89

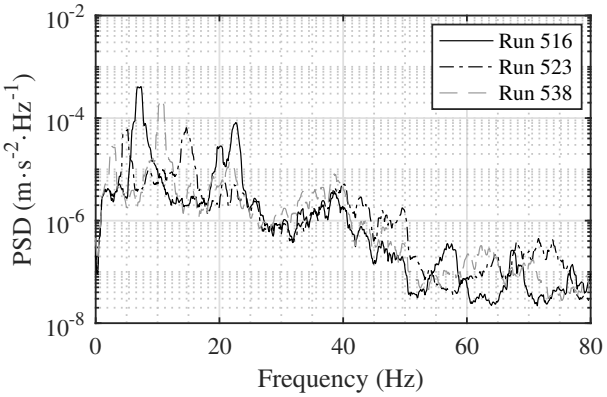

Figure 23: PSD analysis for three white noise tests

the ability of the WN12 signal to actually activate the two first eigenmodes and to give reliable eigenfrequencies values since they are in good agreement with hammer test results.

Then, a higher PGA white noise is sent to the shaking table. The maximum displacement reached by the mid-span point during the run 543 is 22.2 mm (figure 27a), which corresponds to a ductility $\mu = 4.3$. Referring to the best fitting curve plotted in figure 20 deduced from quasi-static cyclic tests, it corresponds to an EVDR of 3.39 %. The confidence in this result is strengthen by the free vibrations logarithmic decrement measured at the end of run 543 that shows a 3.44 % EVDR (figure 26). The same procedure is applied on the 2nd projected displacement (figures 28a and 28b), but the signal over noise ratio is way less favorable and the free vibrations regime less readable.

An alternative method to identify damping ratios and first eigenfrequencies is to apply the minimization process described in section 3.6 and figure 9 on successive time windows. A time window duration of 200 milliseconds proved to be adequate regarding the error criterion in this case. In order to regularize the procedure, the relative variation of identified parameters between two successive time windows is constrained at a maximum of 10 %. A deeper description of the method will be given in a companion paper, and a somehow analogous work have been carried out by Demarie and Sabia [15]. The results (figures 29a and 30a) exhibit a relatively high scatter on the EVDR (mean value of 3.07 % for a standard deviation of 2.29 %). Also, the first eigenfrequency (2.87 Hz with a standard deviation of 0.51 Hz) remains almost unchanged during the run 543. However, focusing on the free vibrations regime, EVDR grows as the amplitude decays, from about 2 % to 6 %, with a mean value of 4.17 %. This value, slightly higher than the one obtained from the LDM and Jacobsen's areas method for the corresponding ductility level, may be overestimated because the decay envelope is steeper on the identified SDOF oscillator than on the

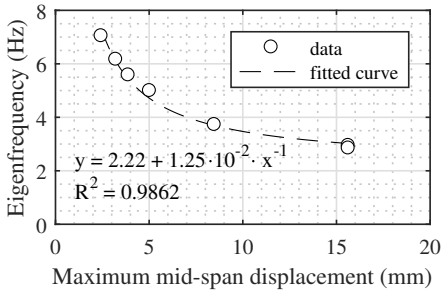

(a) 1st eigenfrequency evolution versus the maximum time-history mid-span displacement

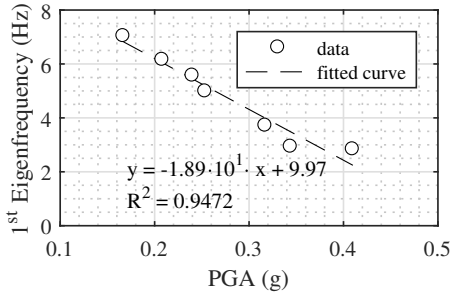

(b) 1st eigenfrequency evolution versus the maximum time-history peak-ground acceleration

Figure 24: Evolution of the 1st eigenfrequency along WN12 tests

experimental projected displacement as observed on figure 27b. It is interesting to note that the error indicator strongly increases when the signal over noise ratio decreases, as it is the case in the last oscillations of the free vibrations regime (after 106 s, figure 31b).

A discordant value, 2.24 %, is given by half-bandwidth method applied on the hammer shock test record (figure 21) which is significantly lower than the values given by the other methods. The half-bandwidth method applied on sixteen different hammer shock tests on beams HA20-C1A showed a standard deviation of around 10 % but this is not sufficient to explain the observed difference. The displacements are way higher in WN12 test than those obtained after a hammer shock and this may explain the difference. Indeed, a previous numerical-experimental study [23] showed that the EVDR successively increases and decreases with respect to the displacement amplitude for a constant ductility level.

Due to the measurement noise, the credit to give to the 2nd eigenmode associated identified values is lower. The general tendency of the EVDR on the 2nd eigenmode is to be higher than the one identified on the 1st eigenmode, i.e. a mean value of 10.1 % for a high standard deviation of 9.77 %. Qualitatively, this result contradicts the conclusions of the half-power bandwidth method (figure 21) which gives a higher damping ratio on the first eigenmode.

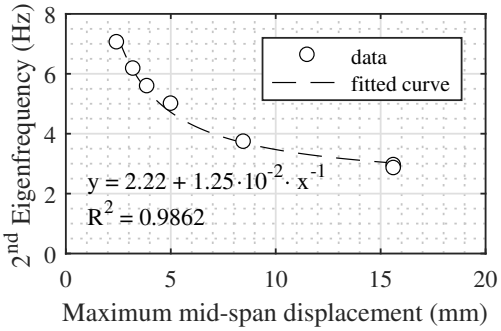

(a) 2nd eigenfrequency evolution versus the maximum time-history mid-span displacement

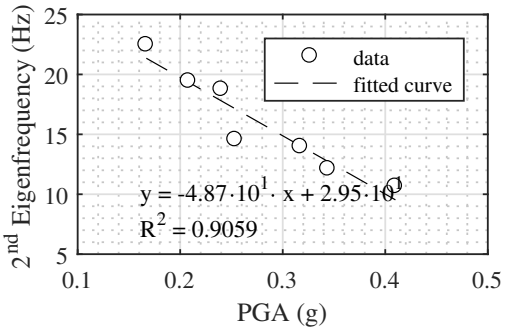

(b) 2nd eigenfrequency evolution versus the maximum time-history peak-ground acceleration

Figure 25: Evolution of the 2nd eigenfrequency along WN12 tests

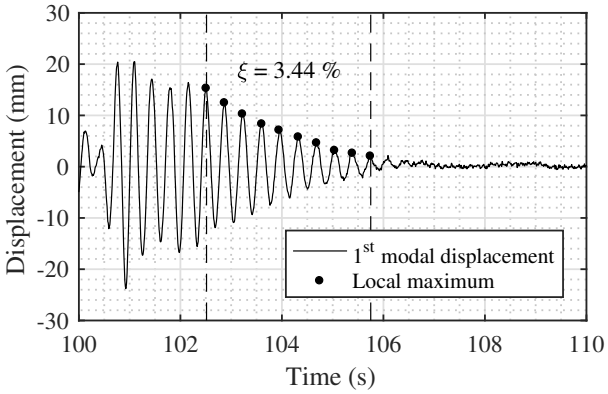

Figure 26: Free vibrations at the end of run 543 (highest acceleration WN12 for the highest damage level) and associated EVDR estimated by LDM

5. Conclusions

A proper evaluation of the energy dissipated by RC structures during seismic events is required to ensure their capability to resist, but this remains a challenging task. The necessity of experimental data to study the damping phenomena has motivated numerous experimental campaign. The present experimental campaign is an attempt to provide further information regarding the evolution of the dissipations throughout time-history analysis, and interactions between modes. Thanks to an innovative design and original optical measurement device, different approaches could have been tested. An improved areas method has been proposed to better account for distorted hysteresis loops, such it is the case with IDEFIX RC beams which exhibit a pinching effect. The experimental setup and the measures proved to be reliable. First results indicate that different methods of equivalent damping ratios evaluation might provide very different results, questioning the applicability framework of all of them. An extended study should help to better understand in which context each method should be used. Many aspects from the tests still have to be studied. Some of them are to be addressed in a companion paper. Aside from this paper, the experimental data will be organized and released in order to make them available to the scientific community by SEISM Institute in the framework of SINAPS@ project (see the acknowledgments for more details).

Acknowledgments

The authors wish to express their most grateful thanks to CEA/DEN for its financial support. The work carried out under the SINAPS@ project has benefited from French funding managed by the National Research Agency under the program Future Investments (SINAPS@ reference No. ANR-11-RSNR-0022). The work reported in this paper has also been supported by the SEISM Institute (http://www.institut-seism.fr).

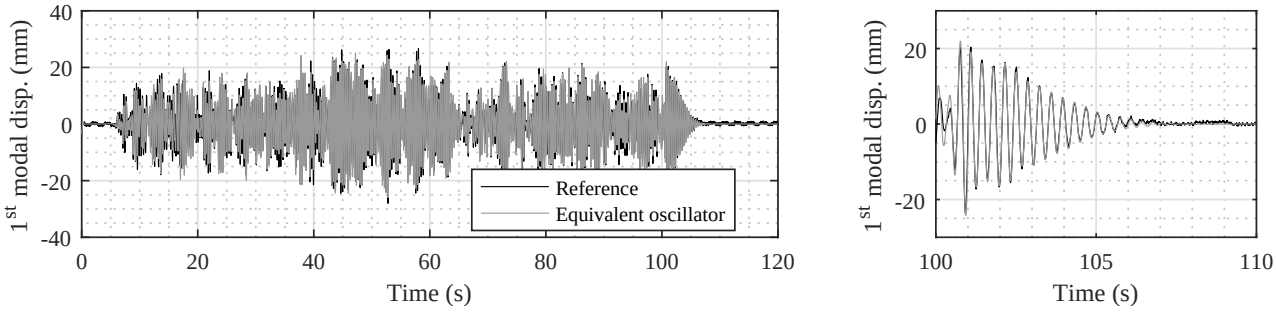

(a) Overall view (b) Zoom on free vibrations regime

Figure 27: 1st modal displacement during run 543 (WN12)

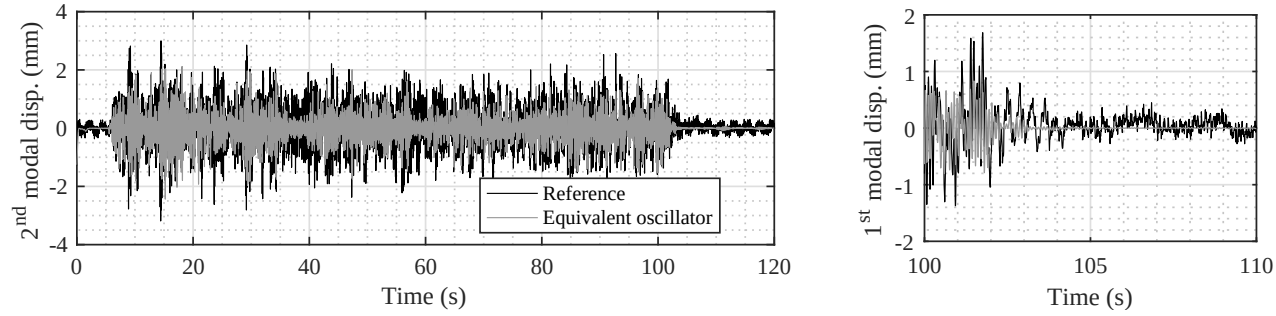

(a) Overall view (b) Zoom on free vibrations regime

Figure 28: 2nd modal displacement during run 543 (WN12)

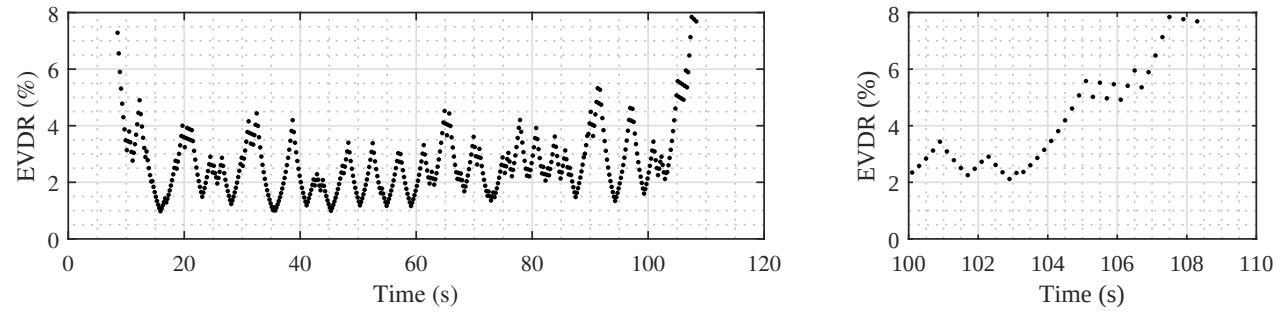

(a) Overall view (b) Zoom on the free vibrations regime

Figure 29: EVDR values identified for 1st eigenmode by sliding time windows (duration of 200 ms) and constrained variations (10 % between two successive values) during run 543 (WN12)

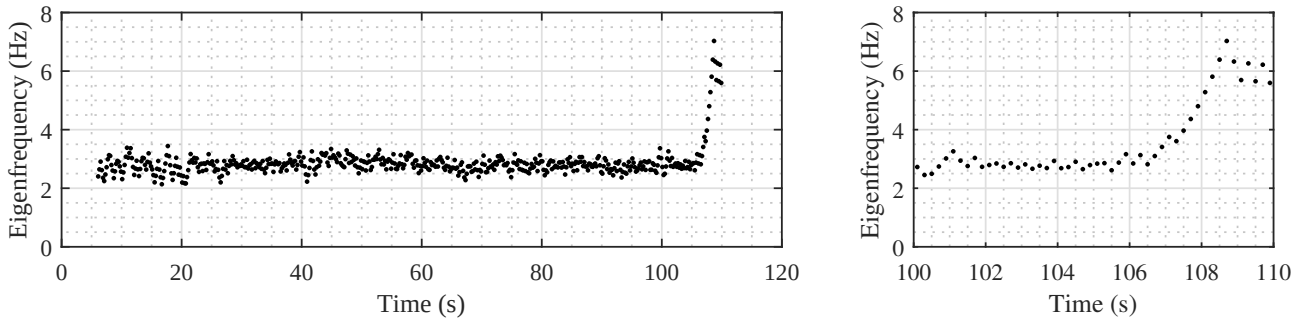

(a) Overall view (b) Zoom on the free vibrations regime

Figure 30: Identified 1st eigenfrequency during run 543 (WN12)

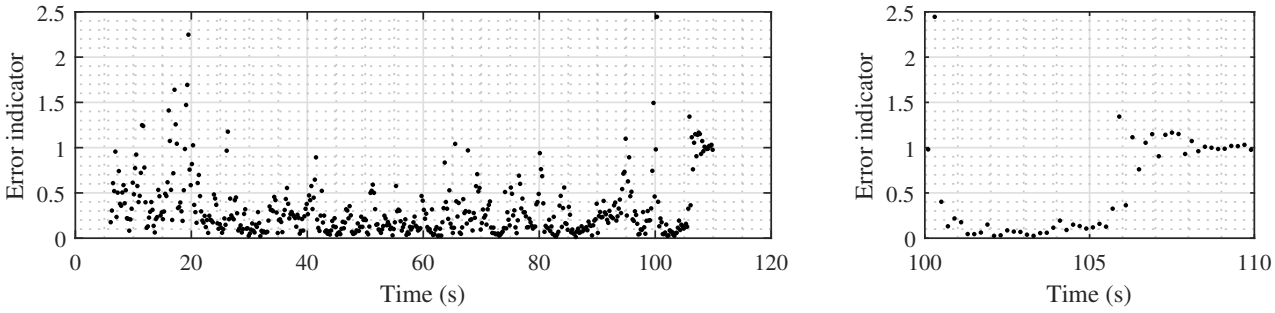

(a) Overall view (b) Zoom on the free vibrations regime

Figure 31: Identification error for 1st eigenmode for run 543 (WN12)

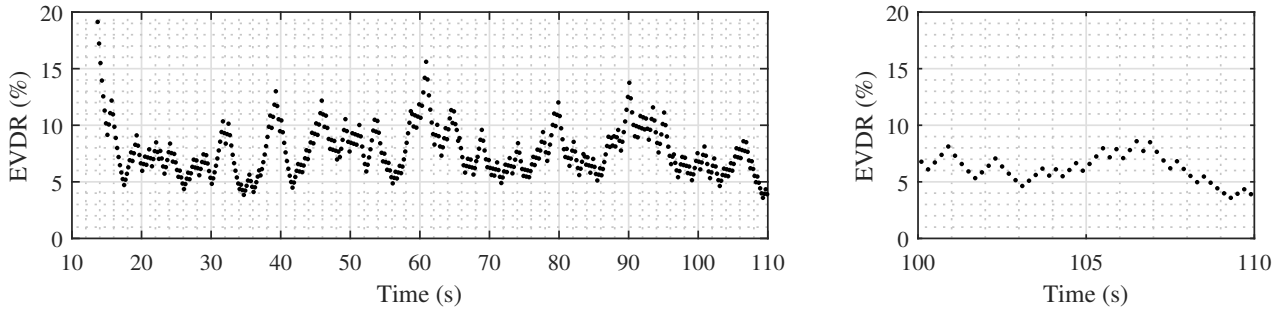

(a) Overall view (b) Zoom on the free vibrations regime

Figure 32: EVDR values identified for 2nd eigenmode by sliding time windows (duration of 200 ms) and constrained variations (10 % between two successive values) during run 543 (WN12)

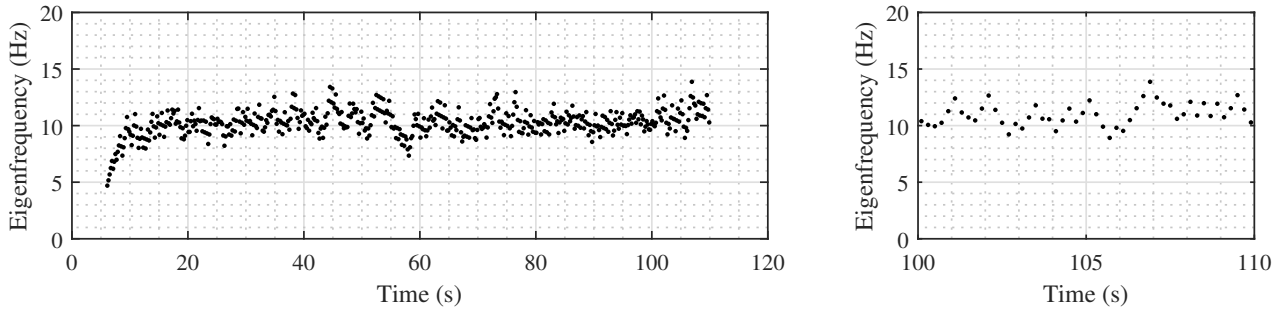

(a) Overall view (b) Zoom on the free vibrations regime

Figure 33: Identified 2nd eigenfrequency during run 543 (WN12)

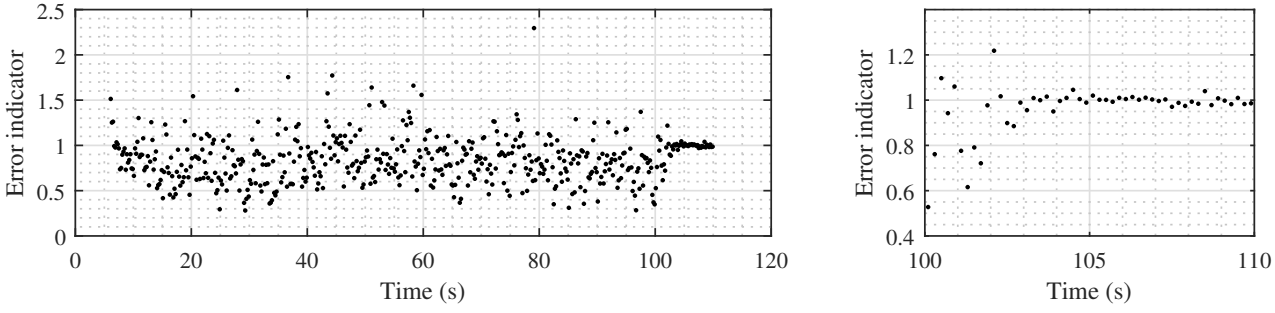

(a) Overall view (b) Zoom on the free vibrations regime

Figure 34: Identification error on 2nd eigenmode for run 543 (WN12)

References

[1] Adhikari, S., Woodhouse, J., 2001. Identification of damping: Part 1, viscous damping. Journal of Sound and Vibration 253 (1), 43–61.

[2] Adhikari, S., Woodhouse, J., 2001. Identification of damping: part 2, non-viscous damping. Journal of Sound and Vibration 243 (1), 63–88.

[3] Angela Salzmann, S. Fragomeni, Y. C. L., 2003. The Damping Analysis of Experimental Concrete Beams under Free-Vibration. Advances in Structural Engineering 6 (1), 53–64.

[4] Asmussen, J. C., 1997. Modal analysis based on the random decrement technique: application to civil engineering structures. Ph.D. thesis, Aalborg Universitet.

[5] Baghiee, N., Reza Esfahani, M., Moslem, K., apr 2009. Studies on damage and FRP strenghening of reinforced concrete beams by vibration monitoring. Engineering Structures 31 (4), 875–893.

[6] Capozucca, R., dec 2009. Static and dynamic response of damaged RC beams strengthened with NSM CFRP rods. Composite Structures 91 (3), 237–248.

[7] Carneiro, J. O., DeMelo, F. J. Q., Jalali, S., Teixeira, V., Tomás, M., sep 2005. The use of pseudo-dynamic method in the evaluation of damping characteristics in reinforced concrete beams having variable bending stiffness. Mechanics Research Communications 33 (5), 601–613.

[8] Caughey, T. K., 1960. Classical normal modes in damped linear dynamic systems. Journal of Applied Mechanics 27 (2), 269–271.

[9] Charney, F. A., 2006. Consequences of using Rayleigh damping in inelastic response history analysis. In: 17th Analysis and Computation Specialty Conference. Universidad de Concepción.

[10] Cole, H. A. J., 1973. On-line failure detection and damping measurement of aerospace structures by random decrement signatures. Tech. rep., NASA.

[11] Comité Européen de Normalisation, 2005. Eurocode 2: Design of concrete structures - Part 1-1: General rules and rules for buildings (February 2015).

[12] Correia, A. A., Almeida, J. P., Pinho, R., 2013. Seismic energy dissipation in inelastic frames: Understanding state-of-the-practice damping models. Structural Engineering International: Journal of the International Association for Bridge and Structural Engineering (IABSE) 23 (2), 148–158.

[13] Crambuer, R., Richard, B., Ile, N., Ragueneau, F., 2013. Experimental characterization and modeling of energy dissipation in reinforced concrete beams subjected to cyclic loading. Engineering Structures 56, 919–934.

[14] Daoud, A., Maurel, O., La Borderie, C., 2013. 2D mesoscopic modelling of bar-concrete bond. Engineering Structures 49, 696–706.

[15] Demarie, G. V., Sabia, D., 2010. Non-linear damping and frequency identification in a progressively damaged R.C. Element. Experimental Mechanics 51 (2), 229–245.

[16] Dunand, F., 2005. Pertinence du bruit de font sismique pour la caracterisation dynamique et l'aide au diagnostic sismiique des structures de génie civil. Ph.D. thesis, Université Joseph Fourier - Grenoble I.

[17] Eligehausen, R., Popov, E. P., Bertéro, V. V., 1982. Local bond stress-slip relationships of deformed bars under generalized excitations. Tech. rep.

[18] Elmenshawi, A., Brown, T., jan 2009. Hysteretic energy and damping capacity of flexural elements constructed with different concrete strengths. Engineering Structures 32 (1), 297–305.

[19] Franchetti, P., Modena, C., Feng, M. Q., 2009. Nonlinear damping identification in precast prestressed reinforced concrete beams. Computer-Aided Civil and Infrastructure Engineering 24 (8), 577–592.

[20] Gulkan, P., Sozen, M. A., 1974. Inelastic responses of reinforced concrete structure to earthquake motions. In: Journal Proceedings. Vol. 71. pp. 604–610.

[21] Hall, J. F., 2006. Problems encountered from the use (or misuse) of Rayleigh damping. Earthquake Engineering and Structural Dynamics 35 (5), 525–545.

[22] Heitz, T., Giry, C., Richard, B., Ragueneau, F., 2017. How are the equivalent damping ratios modified by nonlinear engineering demand parameters? In: 6th International Conference on Computational Methods in Structural Dynamics and Earthquake Engineering. Rhodes Island.

[23] Heitz, T., Richard, B., Giry, C., Ragueneau, F., Le Maoult, A., 2017. Damping identification and quantification: experimental evidences and first numerical results. In: 16th World Conference on Earthquake Engineering. Santiago de Chile.

[24] Hild, F., Roux, S., Gras, R., Guerrero, N., Marante, M. E., Flórez-López, J., 2009. Displacement measurement technique for beam kinematics. Optics and Lasers in Engineering 47 (3-4), 495–503.

[25] Institut-SEISM, ???? SINAPS@.
URL http://www.institut-seism.fr/en/projects/sinaps/

[26] Iwan, W. D., Gates, N. C., 1979. The effective period and damping of a class of hysteretic structures. Earthquake Engineering and Structural Dynamics 7 (3), 199–211.

[27] Jacobsen, L. S., 1930. Steady forced vibration as influenced by damping. Transactions of ASME 52, 169–181.

[28] Jacobsen, L. S., 1960. Damping in composite structures. Proceedings of the 2nd world conference on on earthquake engineering 2, 1029–1044.

[29] Jehel, P., 2014. A critical look into Rayleigh damping forces for seismic performance assessment of inelastic structures. Engineering Structures 78, 28–40.

[30] Jehel, P., Léger, P., Ibrahimbegovic, A., 2014. Initial versus tangent stiffness-based Rayleigh damping in inelastic time history seismic analyses. Earthquake Engineering and Structural Dynamics 43, 467–484.

[31] Kowalsky, M. J., 1994. Displacement based design: a methodology for seismic design applied to RC bridge columns. Tech. rep., University of California, San Diego, California.

[32] Kumar, S. S., Krishna, M., Dey, A., 2015. Cyclic Response of Sand Using Stress Controlled Cyclic Triaxial Tests. 50th INDIAN GEOTECHNICAL CONFERENCE (December).

[33] Li, Q. S., Yang, K., Zhang, N., Wong, C. K., Jeary, A. P., 2002. Field measurements of amplitude-dependent damping in a 79-storey tall building and its efects on the structural dynamic responses. The Structural Design of Tall Buildings 11 (2), 129–153.

[34] Liu, K. S., Tsai, Y. B., 2010. Observed natural frequencies, damping ratios, and mode shapes of vibration of a 30-story building excited by a major earthquake and Typhoon. Earthquake Spectra 26 (2), 371–397.

[35] Michel, C., Guéguen, P., Bard, P.-Y., 2008. Dynamic parameters of structures extracted from ambient vibration measurements: An aid for the seismic vulnerability assessment of existing buildings in moderate seismic hazard regions. Soil Dynamics and Earthquake Engineering 28 (8), 593–604.

[36] Ndambi, J., Peeters, B., Maeck, J., De Visscher, J., Wahab, M., Vantomme, J., De Roeck, G., De Wilde, W., 2000. Comparison of techniques for modal analysis of concrete structures. Engineering Structures 22 (9), 1159–1166.

[37] Ouglova, A., Berthaud, Y., Foct, F., François, M., Ragueneau, F., Petre-Lazar, I., jun 2008. The influence of corrosion on bond properties between concrete and reinforcement in concrete structures. Materials and Structures 41 (5), 969–980.

[38] Perera, R., Huerta, C., Orquín, J. M., 2007. Identification of damage in RC beams using indexes based on local modal stiffness. Construction and Building Materials 22 (8), 1656–1667.

[39] Priestley, M. J. N., 2003. Myths and fallacies in earthquake engineering, revisited. IUSS press.

[40] Priestley, M. J. N., Calvi, G. M., Kowalsky, M. J., 2007. Displacement-based seismic design of structures. In: NZSEE Conference. Vol. 23. pp. 1453–1460.

[41] Reynolds, P., Pavic, A., may 2000. Impulse hammer versus shaker excitation for the modal testing of building floors. Experimental Techniques 24 (3), 39–44.

[42] Richard, B., Fontan, M., Mazars, J., 2014. SMART 2013: Overview, synthesis and lessons learnt from the International Benchmark. Tech. rep.

[43] Richard, B., Martinelli, P., Voldoire, F., Chaudat, T., Abouri, S., Bonfils, N., 2016. SMART 2008: Overview, synthesis and lessons learned from the International Benchmark. Engineering Structures 106, 166–178.

[44] RILEM TC, 1994. RC 6 Bond test for reinforcement steel. RILEM Recommendations for the testing and use of constructions materials (1983), 218–220.

[45] Rodrigues, H., Varum, H., Arêde, A., Costa, A., 2011. A comparative analysis of energy dissipation and equivalent viscous damping of RC columns subjected to uniaxial and biaxial loading. Engineering Structures 35, 149–164.

[46] Rosenblueth, E., Herrera, I., 1964. On a kind of hysteretic damping. Journal of Engineering Mechanics (90), 37–48.

[47] Satake, N., Suda, K.-i., Arakawa, T., Sasaki, A., Tamura, Y., 2003. Damping evaluation using full-scale data of buildings in Japan. Journal of Structural Engineering 129 (4), 470–477.

[48] Videometric, ???? Videometric.
URL http://www.videometric.com/en/